ADVANCED FUNCTIONAL MATERIALS
www.afm-journal.de

Tuneable Topography and Hydrophobicity Mode in Biomimetic Plant-Based Wax Coatings

*Francis J. Dent, Gunjan Tyagi, Faye Esat, João T. Cabral, and Sepideh Khodaparast**

Across diverse natural surfaces, remarkable interfacial functionalities emerge from micro and nanoscale self-assemblies of wax components. The chemical composition of the epicuticular wax prescribes the intrinsic crystal morphology and resultant topography of the natural surfaces, dictating their interfacial wetting properties. The potential of regulating the topography of identical wax compositions through various crystallization routes is tested here. Crystallization through solvent evaporation produces diverse topographies with enhanced surface hydrophobicity compared to the slow cooling of the wax melt. Further, the microscale interfacial crystalline structure can be deliberately designed to operate in *sticky* or *slippery* hydrophobic regimes through control of the supersaturation level during the crystallization process. While the supersaturation level significantly impacts surface wettability by modulating the microscopic aggregation of rice bran wax crystals, the crystal structure at the molecular scale remains effectively unchanged. The relationships between the supersaturation level, surface topography and hydrophobicity modes, primarily derived for rice bran wax, are qualitatively validated for a wider range of plant-based waxes. Crystallization of inherently hydrophobic plant-based waxes from thermodynamically isotropic solutions offers an affordable single-step approach for the fabrication of biodegradable hydrophobic coatings, applicable to versatile materials and geometries.

1. Introduction

Water-repelling surfaces have found growing applications in diverse emerging technologies, ranging from corrosion-resistant coatings[1] to antibacterial fabrics.[2] Extreme hydrophobic properties[3] are often achieved in systems of complex physical topographies and low surface energy.[4–8] Larger macroscopic contact angles (⩾150°) of water droplets on rough substrates are generally associated with superhydrophobicity in static conditions. However, dynamic conditions are necessary to establish which of the two general wetting regimes may occur, depending on the wetting at micro/nano-scales:[9,10] (i) in the so-called Wenzel state[11] water penetrates within the micro/nano-cavities on the surface. According to the Wenzel wetting formulation, the water contact angle increases with increasing the surface roughness for hydrophobic materials, while the surface wettability is improved when generating roughness in hydrophilic materials. Due to the complete infiltration of water within the cavities, large contact angle hysteresis is observed under dynamic conditions in the Wenzel regime, manifested as *sticky* behavior.[9,12,13] (ii) Contrary to the impaled droplets in the Wenzel state, the droplets sit on a relatively defect-free air cushion due to the air entrapment within the surface roughness[14,15] in the Cassie-Baxter state.[16] The composite air-solid interface reduces the adhesion of the drop, rendering the surface *slippery* with minimal sliding/rolling resistance. In practice, transitional Cassie-Baxter and Wenzel regimes leading to various modes of partial water infiltration are often reported for regular micropatterned surfaces.[13,17,18] Recent micro/nano-fabrication technologies have further extended the wetting regimes, defining a spectrum of wetting behaviors beyond the classic Wenzel and Cassie-Baxter modes through the development of hierarchical and Janus structures.[8,17,19–23] While great progress toward innovative micro/nano-fabrication methods for controlling the surface wetting behavior has been made in the past decades,[5,24] the majority of superhydrophobic surfaces involve fabrication through conventional microfabrication and lithography techniques and/or chemical modifications with fluorination.[7,8,25] To date, the discovery of sustainable materials and affordable manufacturing methods for scalable fabrication of functional

F. J. Dent, S. Khodaparast
School of Mechanical Engineering
University of Leeds
Leeds LS2 9JT, UK
E-mail: s.khodaparast@leeds.ac.uk
G. Tyagi, J. T. Cabral
Department of Chemical Engineering
Imperial College London
London SW7 2AZ, UK
F. Esat
School of Chemical and Process Engineering
University of Leeds
Leeds LS2 9JT, UK

The ORCID identification number(s) for the author(s) of this article can be found under https://doi.org/10.1002/adfm.202307977

DOI: 10.1002/adfm.202307977

hydrophobic coatings remains an active field of academic and industrial research.[26–31]

Inspirations for the design and fabrication of surfaces with desired fluid-handling functionalities have been largely drawn from natural models.[32] The abundance of plant leaves displaying interesting wetting behavior has guided the majority of development in the field since the discovery of the lotus effect.[25,33–36] The combined effect of surface chemistry and physical topography often defines the surface wettability in external plant surfaces.[33,37,38] Successful attempts to regenerate similar structures in the laboratory by recrystallizing waxes extracted from plant leaves have been reported in the literature.[39–41] Recrystallization of epicuticular leaf waxes was studied following thermal[42] and solvent[40] evaporation approaches. The chemical composition of the waxes, presence of impurities, and substrate crystallinity were found to be most influential on the final nano-topographies obtained.[40,43] In comparison, the impacts of physical environmental conditions such as temperature, pressure, and factors influencing the rate of crystallization have not yet been systematically investigated despite earlier findings suggesting the significant impact of solvent and temperature on the crystal habit.[40] The low surface energy of waxes derived from various plant-based resources and opportunities for inducing diverse micro/nano-structures offer potential biomimetic routes for scalable fabrication of functional hydrophobic coatings.[26,44] To attain the effective combined properties, crystallization approaches including solidification through cooling,[4] emulsification,[27,45,46] solvent evaporation,[40,47] and thermal evaporation[48,49] have proven successful. While crystallization of naturally hydrophobic waxes appears as a promising route for the fabrication of water-repelling coatings, deterministic design and control of the wax self-assemblies toward desired wetting regimes is yet to be realised.

Natural *sticky* hydrophobic surfaces often collect environmental dew in plants and insects,[50–53] while man-made mimics have proven effective in applications such as anti-splashing coatings, water harvesting and condensation cooling.[22,54,55] On the other hand, the *slippery* Cassie-Baxter wetting condition is commonly exploited to generate *self-cleaning* effects inspired by the lotus leaf, harnessing the ability to dispose of surface contamination and stains using interfacial capillary-driven forces.[35,56] Current technologies are developed to achieve either *slippery* or *sticky* behavior by modifying the fabrication techniques and/or material in use, often involving a combination of top-down and bottom-up manufacturing methods.[42,54,57–60] Here, we investigate the efficacy of wax crystallization approaches for the fabrication of hydrophobic surfaces exhibiting tuneable *slippery* or *sticky* behaviors by controlling the micro/nano-scale crystal structures. We test the idea of organising the nanoscale crystals of a given wax into self-assemblies of different micromorphologies to achieve diverse wetting regimes in chemically identical materials. Plant-based waxes are used, allowing for large-scale fabrication of nanostructured superhydrophobic coatings from available bio-resources.[61] We investigate the influence of solvent and temperature on the topographies generated through the crystallization process and the effect on the corresponding surface wettability mode. We perform a series of analytical measurements to characterize the structure, melting temperature, and composition of the various wax crystals produced through the cooling and evaporation of diverse solvents. This investigation will mainly focus on the wax extracted from rice bran oil, with core findings briefly tested in other similarly resourced natural waxes. Exploring various natural waxes and the diversity of their crystalline structures not only allows progress in fundamental understandings of natural bio-resources, but offers affordable routes for the biomimetic design and fabrication of functional materials.

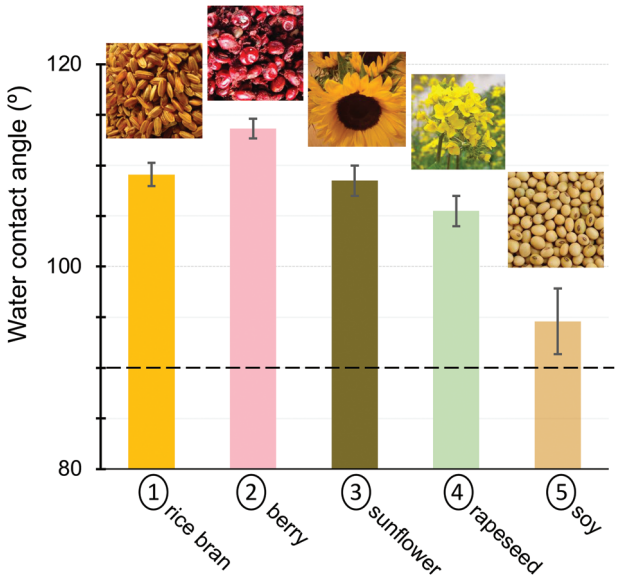

Figure 1. Water contact angles of 3 µL droplets deposited on coatings generated via cooling of the wax melts at 24 °C. The dashed line refers to the 90 °C hydrophilic–hydrophobic separation distinction. Rice bran wax is extracted from the rice bran oil. Sunflower, rapeseed and soy waxes are extracted from the oil derived from the grains. Berry wax is extracted from the peels of berries of the *Rhus verniciflua* tree.

2. Results and Discussion

Wetting behavior of crystallized wax-based coatings is a function of thechemistry and topographic nano/micro-structure of the wax crystals.[39] To identify the impact of physical topographies independently of the wax composition, we characterize the intrinsic wetting behavior of waxes before establishing routes for generating additional surface roughness and analyzing their impact on the wetting behavior.

2.1. Intrinsic Wetting Properties

The plant-based wax coatings were generated by cooling molten rice bran, berry, sunflower, rapeseed, and soy wax pellets at room temperature. All tested waxes exhibited hydrophobic properties with water contact angles greater than or equal to 90°, see **Figure 1**. Cooling resulted in relatively smooth surfaces (Figure S3, Supporting Information), therefore, the observed hydrophobicity and measured contact angles presented in Figure 1 can be considered as the intrinsic properties of the tested waxes.

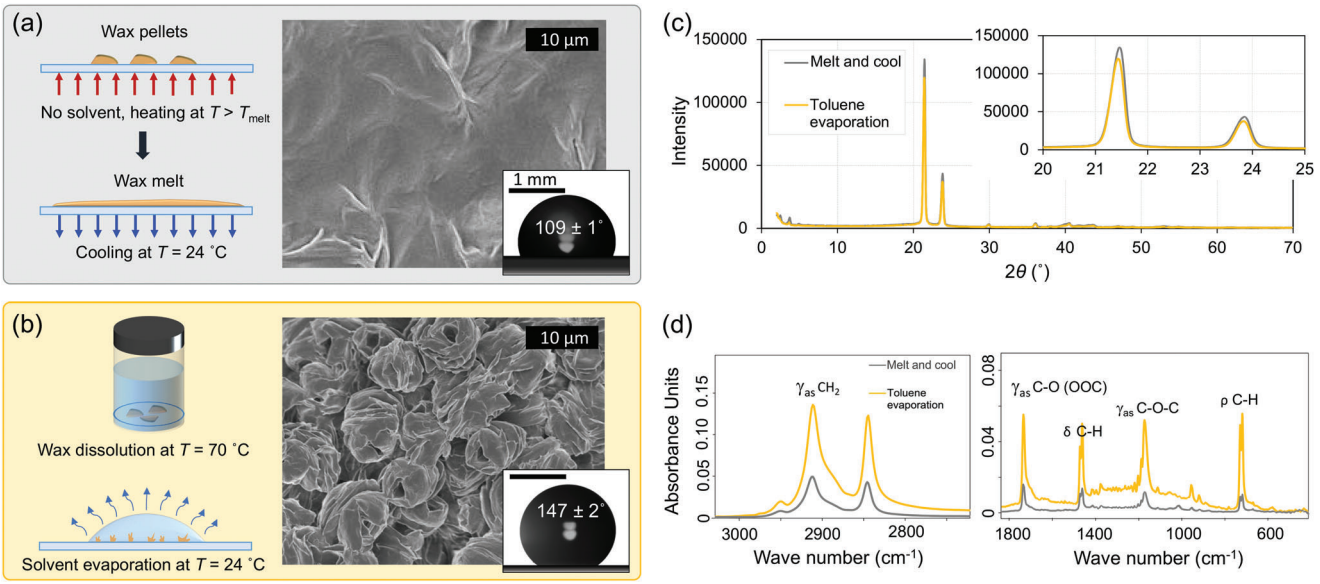

Figure 2. Modification of the surface roughness and subsequent hydrophobicity in rice bran coatings. Schematic of coating methods with respective scanning electron microscopy (SEM) images of surfaces made of rice bran wax, crystallized through (a) cooling and (b) solvent evaporation. c) X-ray diffraction (XRD) signal for the two coatings achieved via cooling and solvent evaporation. d) Comparative attenuated total reflectance (ATR) measurements on rice bran coatings, presented in (a) and (b), show no significant shift in the absorbance peaks. γ_{as}, δ, and ρ correspond to asymmetric stretching and bending (scissoring and rocking) vibrations, respectively.

2.2. Surface Topography

Establishing surface roughness in such naturally hydrophobic waxes is expected to enhance the surface hydrophobicity.[4,12,62] Herein, we mainly focus on generating and modulating surface topographies through crystallization via cooling and solvent evaporation. The resulting surface topographies and crystal structures are discussed. Results and discussions are initially reported for rice bran wax, describing the impact of surface topography on the wettability of the coatings generated on smooth glass substrates. Crystallized coatings of other plant-based waxes are then qualitatively tested for comparison.

2.2.1. Solvent Evaporation Versus Cooling

The crystallization of the wax melt via cooling at room temperature yielded fairly smooth surfaces (**Figure 2**a), whilst solvent evaporation generally induced varied physical topographies (Figure 2b) at the interface. Using toluene as the solvent consistently generated fractal micro-roses with average diameters of around 5 µm made up of curved petals of approximately 100 nm thickness (Figure S4, Supporting Information). The resultant surface roughness was observed to significantly enhance the hydrophobicity of the wax coating, increasing the water contact angle by around 35% with respect to the coatings generated through the cooling of the wax melt.

X-ray diffraction (XRD) analysis of the crystals obtained through cooling and solvent evaporation exhibited no significant variation in the crystal structure or the exact location of the diffraction peaks despite the distinctive surface topographies (Figure 2c). The two intensive wide-angle diffraction peaks (at $2\theta > 20°$) correspond to d-spacing values of 4.14 Å and 3.73 Å, characteristic of orthorhombic structures in aliphatic compounds.[33,63] Due to the presence of different molecules, the long-spacing peaks ($2\theta < 5°$) associated with layer spacing are significantly less intense (Figure S5, Supporting Information).[64] Differential scanning calorimetry (DSC) measurements of the crystalline materials also obtained effectively unchanged melting points at 74.2 ± 0.3°C, complementing the XRD data (Table S1, Supporting Information). In line with XRD and DSC comparative measurements, IR absorbance spectrum collected from the two crystallized coatings demonstrated peaks at identical wave numbers, Figure 2d. The spectra confirm the absence of any solvent traces (toluene in this example) in the coating. These initial findings demonstrate that the crystallization route regulates surface wettability through modulation of the microscopic aggregation of rice bran crystals without significantly impacting their crystalline structures.

Considering the approximate 74 °C melting point of the rice bran wax used in our study (Table S1, Supporting Information), we investigated the impact of elevated casting temperatures, $T_{casting}$, during the wax crystallization via solvent evaporation (**Figure 3**). Rice bran wax was dissolved in toluene at 70°C and subsequently drop-cast on the substrate at the casting temperature, $T_{casting}$. Samples were kept at $T_{casting}$ for one hour to allow full evaporation of the solvent before returning to the ambient conditions. Distinct micro-structures and contact angles were identified in the two regimes dominated by solvent evaporation ($T_{casting} \leq 40°C$) and cooling ($T_{casting} \geq 60°C$), with a transitional region at intermediate temperatures of $T_{casting} \approx 50°C$ (Figure 3). Higher casting temperatures generally improve the solubility of the wax in the solvent.[65] The reduced supersatura-

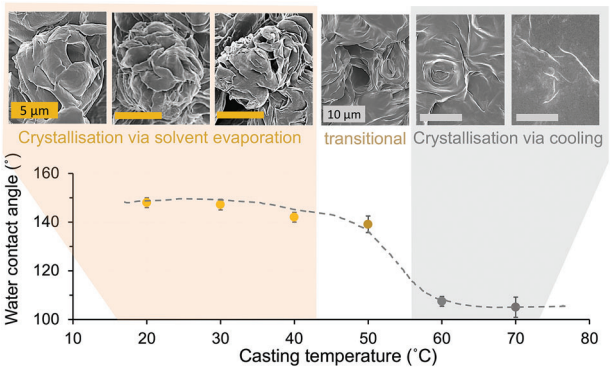

Figure 3. Impact of casting temperature on the surface topography and wettability for coatings fabricated via solvent evaporation from solutions of rice bran wax in toluene. Wax solutions were drop-cast onto substrates and held at the casting temperature for one hour before returning to room temperature.

tion level thus decelerates the crystallization process, especially with $T_{casting}$ close to the melting point.[66] Therefore, crystallization is mainly induced through cooling at room temperature after the faster evaporation of the solvent[67] at $T_{casting} \geq 60$ °C, resulting in relatively smooth surfaces with microscopic wrinkles. For $T_{casting} \geq 60$ °C, micro-structure and contact angle measurements of rice bran wax, crystallized from the evaporation of toluene, were similar to those obtained in the absence of solvent, compare Figure 2a with Figure 3. In contrast, wax crystallization at lower casting temperatures is mainly controlled by the evaporation of solvent at $T_{casting}$ prior to the return to room temperature. For the range of temperatures studied here, crystallization of rice bran wax from toluene yielded the highest water contact angle when drop-cast at temperatures between 20–30 °C.

Exposure to higher temperatures after complete evaporation of the solvent did not have a significant effect on the surface wettability of coatings; crystallized rice bran wax coatings from solutions in toluene maintained average contact angles ranging from 147–150° when heated at higher temperatures that were below the melting point of the wax (Figure S6, Supporting Information).

With solvent evaporation inducing complex micro/nanoscale surface roughness that clearly enhance the surface hydrophobicity, a critical question remains to be answered: "Can the topography and the resulting surface wettability be furthe tuned without modifying the chemical composition of the wax?" In what follows, we discuss the impact of solvent on the result of crystallization through solvent evaporation on the surface.

2.2.2. Choice of Solvent

The supersaturation level impacts the population and size of crystals formed through solvent evaporation by regulating the contribution of nucleation and growth processes. Higher supersaturation levels reduce the induction time while increasing the crystal nucleation rate, in turn generating smaller crystals at larger number density. In contrast, crystallization is largely dominated by growth at low saturation levels, yielding larger crystals with secondary orders.[66,68] Here, we qualitatively control the level of supersaturation by altering the wax solubility and the evaporation rate of the solvent.

Toluene provides good solubility for 10 wt% of rice bran wax at room temperature, therefore, its slow evaporation (over hours) provides continuous crystallization at lower supersaturation levels. In contrast, acetone is a poor solvent for rice bran wax. It evaporates rapidly, i.e., order of seconds after drop-casting, resulting in a spontaneous transition to highly supersaturated levels. Example scanning electron microscopy (SEM) and laser scanning confocal microscopy (LSCM) images of the micro-structures obtained for rice bran wax crystallized from the evaporation of toluene and acetone are presented in **Figure 4**a,b, respectively. The line graphs represent the main characteristic features of each coating, namely the micro-rose in Figure 4a and the petals in Figure 4b. As predicted, the crystals emerging through the evaporation of toluene are relatively larger than those obtained from the evaporation of acetone. LSCM measurements reveal maximum local peak-to-valley distances of around 5 μm from aggregated petals in the form of micro-roses (4–8 μm diameters), which are the microscopic building blocks of the coatings obtained from toluene (Figure 4a). In the acetone-evaporated samples, significantly shorter local peak-to-valley distances of around 1 μm appeared in the form of randomly packed, deformed plates resembling rose petals, see Figure 4b. The individual deformed petals in both morphologies are of approximately 100 nm thickness (see Figures S4 and S7, Supporting Information). We note that petals in acetone-evaporated samples are arranged in different orientations, leading to noticeable topographic variations in close-up images captured using SEM and LSCM on different sections of the sample.

2.3. Wetting Behavior

The topographic micro-structures of rice bran crystals derived from the evaporation of toluene and acetone are distinct in size and form, resulting in observable differences in the wetting behavior of the surface. To further tune the surface topography of the coatings, we tested a series of rice bran wax coatings crystallized from solutions with binary mixtures of acetone and toluene as solvents (**Figure 5**a). The weight percentage of acetone in the solvent, quantified by $\alpha = \frac{\text{acetone}}{\text{acetone+toluene}}$, was systematically increased to achieve diverse surface topographies. Increasing the toluene content in the binary solvent mixture improves the solubility of the wax and reduces the solvent vapor pressure.[69] Consequently, the crystallisation rate was reduced resulting in the formation of larger micro-roses, indicative of the lower supersaturation regime (Figure 5a).

Water contact angle measurements were used to determine the impact of topographic structures on the wetting behavior of the coatings in static conditions. Additionally, two different sliding angles were measured to characterize the wetting behavior of crystallized coatings in the dynamic conditions, (Figure 5b): (i) the static sliding angle refers to the tilt angle at which a slowly deposited droplet slides or rolls down the angled substrate with no major pinning, while (ii) the kinetic sliding angle refers to a tilting angle at which a droplet rolls down or bounces off the surface when released from a distance above the angled substrate

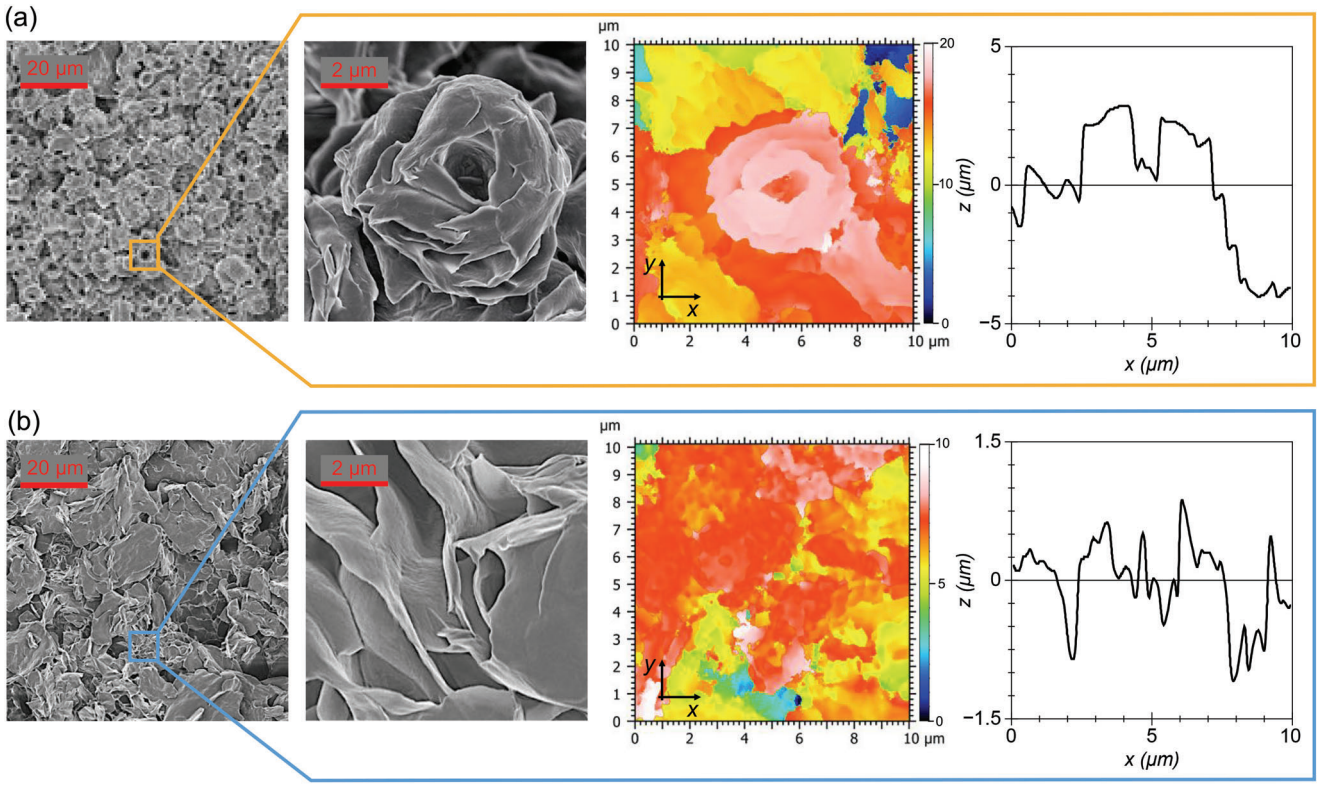

Figure 4. SEM and LSCM images showing the diverse surface topographies obtained through crystallization of rice bran wax from evaporation of (a) toluene and (b) acetone. Graphs show examples of surface features' height (z-axis) along the x-axis. The line graphs represent the main characteristic features of each coating, being the micro-rose in (a) and the petals in (b).

(here 30 mm). The droplet impacted the surface with an approximate velocity of 0.1 ms^{-1}, corresponding to a low Weber number regime in which inertial effects are insignificant.[70] No differentiation between the rolling and bouncing dynamics is considered here.[71] The two static and kinetic sliding tests were performed to highlight the impact of the droplet deposition method, modelling different modes of interaction with water droplets in nature[35,58,72–74] and engineering applications.[19,75–77]

2.3.1. Sticky Versus Slippery Coatings

Accelerated crystallization achieved at higher supersaturation levels, denoted here by a larger α value, generally increased the hydrophobicity of the samples. Acetone-evaporated rice bran wax samples (α = 100%) exhibited relatively larger static water contact angles in comparison to toluene-evaporated samples (α = 0%), measuring around 160° compared to 147°, respectively (Figure 5c). Interestingly, two distinct dynamic wetting regimes were found for the rice bran wax coatings when the slow-evaporating toluene was substituted by the fast-evaporating acetone, see Figure 5c. The acetone-evaporated surfaces appear slippery with small sliding angles (<5°), yielding self-cleaning properties characteristic of the *lotus leaf*.[35] While relatively large static water contact angles (⩾150°) were achieved on both surfaces, the toluene-evaporated surface exhibited high adhesion of the droplets often referred to as the *rose petal* or *parahydrophobic* effect.[23,58,78] The higher resistance of the contact line to motion and strong pinning effects are maintained in both static and kinetic sliding angle measurements for toluene-evaporated coatings. This is demonstrated by the increasing trend in sliding angle for kinetic tests (droplet impact) and the inability to measure any static sliding angles for surfaces of $\alpha \leq 25\%$ (Figure 5c). Further observations of the relative pinning effects between acetone- and toluene-evaporated surfaces can be viewed in supplementary Videos S1 and S2 (Supporting Information).

The transition between the two regimes was gradual and variations of morphology and wettability states were observed when mixtures of acetone and toluene were used as solvents. Both kinetic and static sliding angles decreased at larger values of α; kinetic sliding angles measured upon droplet impact were significantly smaller than classical static sliding measurements. This finding suggests that the observed rose petal effect is caused by severe contact line pinning, potentially resulting from partial impalement of water droplets through the larger cavities in static conditions (Figure 4a) present on the toluene-evaporated surfaces, rather than complete Wenzel state of wetting.[23] Despite the significantly diverse micro-structures found when using different mixed-solvent compositions, XRD, ATR, and DSC measurements for crystals grown via evaporation of toluene, acetone and mixtures at α = 50% showed no distinctive structural difference at the molecular scale, in comparison to crystals grown from cooling of the wax melt (Table S1 and Figure S8, Supporting Information).

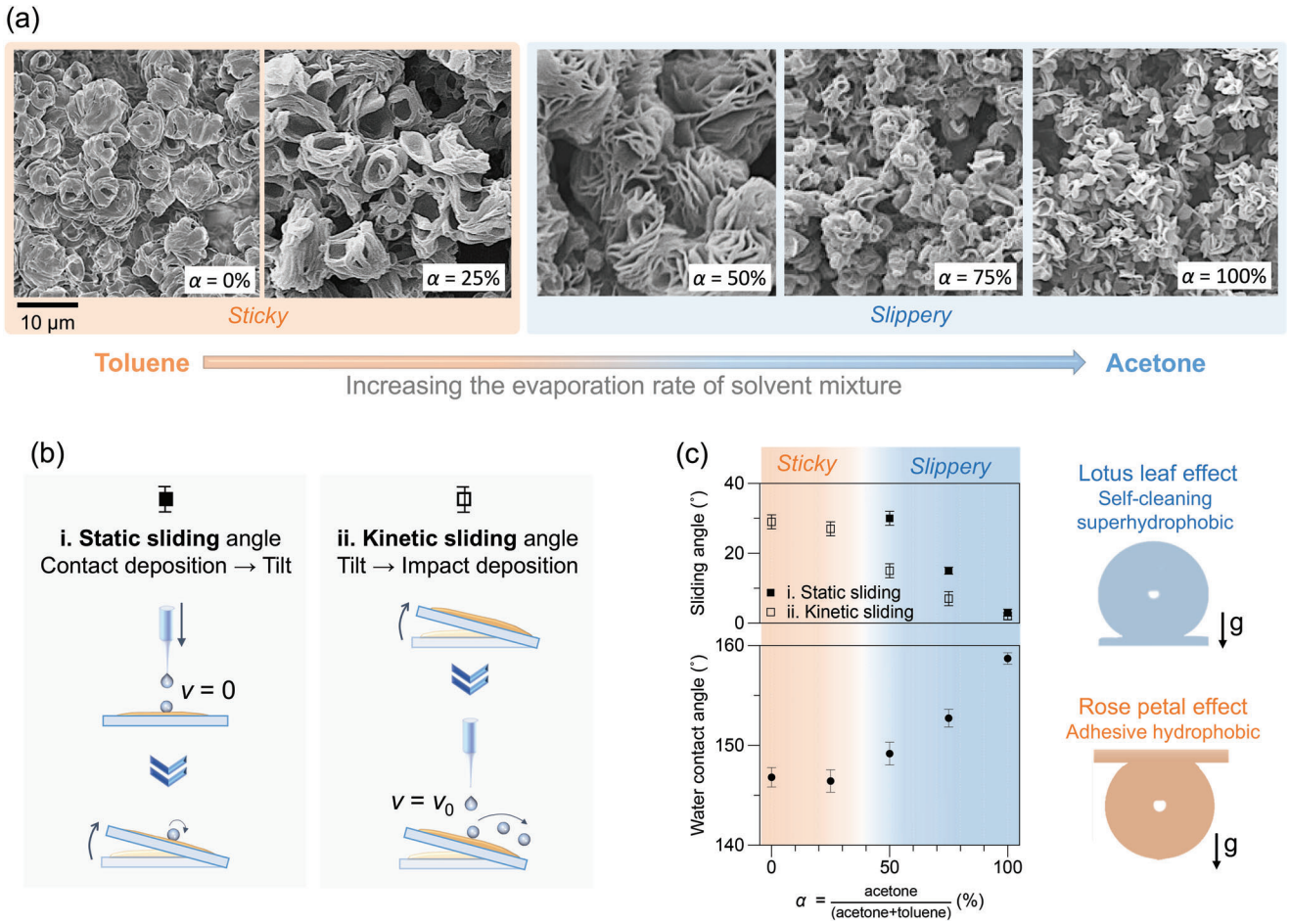

Figure 5. Surface topography and wettability for rice bran coatings crystallized through the evaporation of mixed solvents, with $\alpha = \frac{\text{acetone}}{\text{acetone+toluene}}$ denoting the relative weight percentage of acetone in the solvent. a) SEM images show the variety of morphologies ranging from closed micro-roses (for 0% acetone) to roses with loose petals (≈ 50% acetone) and finally to isolated petals (100% acetone). Scale bar refers to 10 μm in all images. b) Static sliding angle refers to the tilt angle at which a droplet, initially deposited on a flat surface, begins to slide. Kinetic sliding angle corresponds to the tilt angle that induces rolling or bouncing when the droplet is released from 30 mm distance. c) Increasing α enhanced surface hydrophobicity manifested in larger static contact angle and smaller sliding angles, while decreasing α yielded relatively smaller water contact angle and higher adhesion. Droplets remained attached to the surface of the coating at $\alpha = 0\%$ and $\alpha = 25\%$ even after the surface was turned upside down, therefore, static sliding angle is not reported for these cases.

The striking co-existence of *sticky* and *slippery* micro/nano-structured coatings was previously reported for surfaces of plants. Surfaces of the leaves and flowers of rapeseed plants showed notably different *sticky* and *slippery* wetting behaviors.[79] On petals of different species of roses, the size and spacing of surface structures were found to engender different hydrophobicity modes on the petals.[58]

2.3.2. Wetting Regimes and Transitions

While the wetting properties of acetone-evaporated coatings were consistently in line with the characteristics of Cassie-Baxter wetting regime, the *sticky* behavior of the toluene-evaporated surfaces remains more challenging to delineate.[23,25,58] Further tests were performed to better identify the wetting regimes and potential transitions on the crystallized rice bran coatings.[70] Comparative sessile droplet evaporation tests were performed on acetone- and toluene-evaporated rice bran coatings (**Figure 6**a). Additionally, droplet squeezing tests were performed by gently pressing sessile droplets on the wax coating using a hydrophobic surface (Figure 6b).

Sessile droplets on hydrophobic and superhydrophobic surfaces undergo different regimes of constant contact angle (CCA) and constant contact radius (CCR) during evaporation.[80] While CCA is indicative of continuous sliding of the contact line on *slippery* surfaces, CCR is characteristic of *sticky* coatings that induce significant pinning of the contact line on the surface. Droplet evaporation on rice bran wax coatings crystallized from acetone is dominated by a semi-CCA mode, during which the average contact angle remains above 150° (Figure 6a,i).[81] The *slippery* wetting behaviour of the coating, exhibiting a continuously retracting baseline diameter of the sessile droplet (Figure 6 aii), is indicative of Cassie-Baxter wetting. The toluene-evaporated

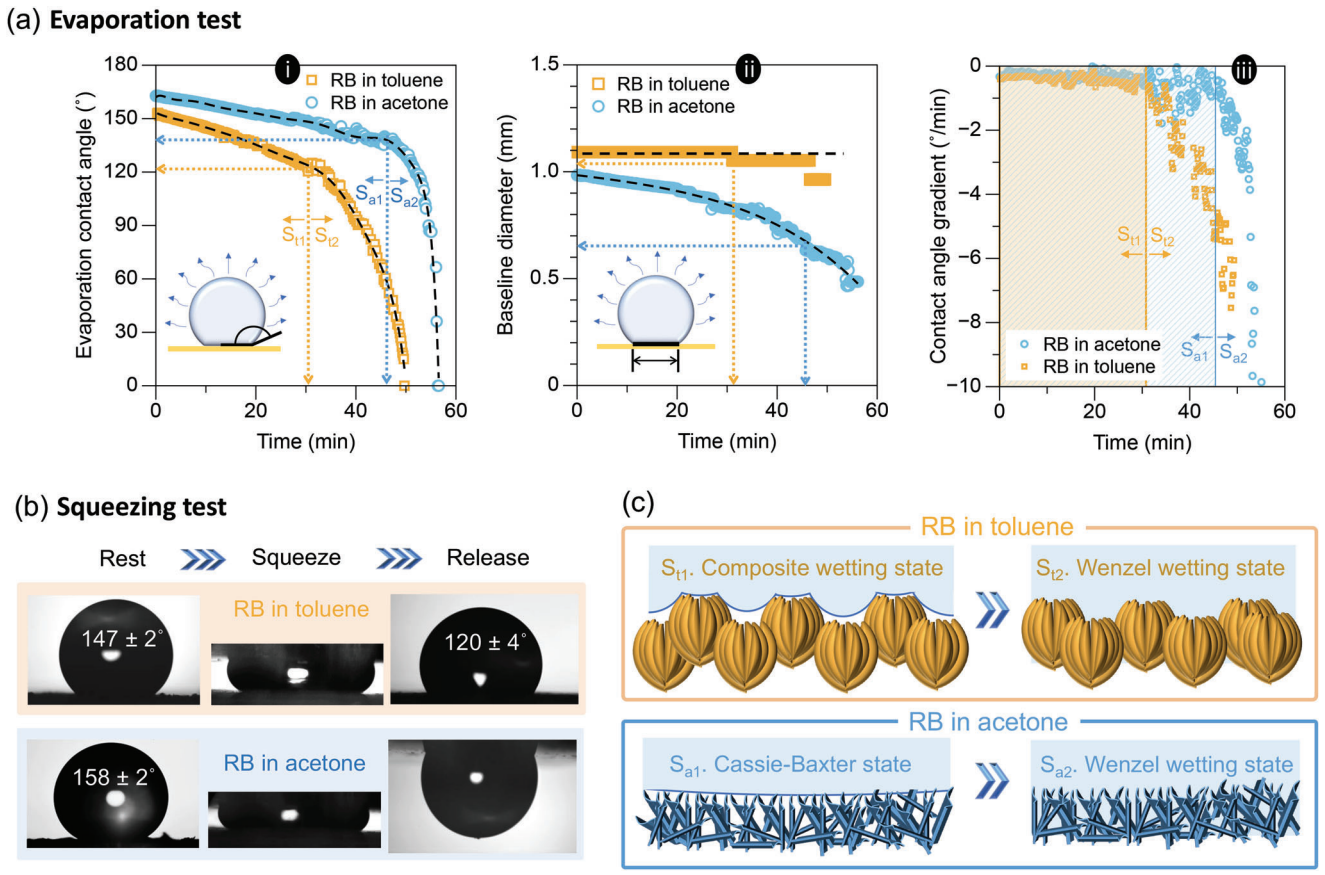

Figure 6. Wetting regimes and transitions. a) **Evaporation test**: Quantitative shape analysis during the evaporation of a 5 µL droplet showing the evolution of (i) average contact angle, (ii) baseline diameter, and (iii) Local gradient of contact angle-time data presented in (i) as a function of time. Graphs highlight the transition between S_1 to S_2 corresponding to non-wetting and wetting, respectively. Subscripts a and t refer to cases involving evaporation of acetone and toluene. b) **Squeezing test**: Wetting behavior of toluene-evaporated (top) and acetone-evaporated (bottom) coatings during squeeze and release test. c) Schematic of the speculated wetting regimes on crystallized rice bran wax coatings. The respective surfaces undergo full transition to Wenzel state where air pockets are replaced by water.

crystalline samples demonstrated characteristic CCR behaviour, denoted by a near-constant contact baseline diameter and continuous decrease in contact angle (Figure 6a,ii). The larger contact angle and smaller baseline contact area on the *slippery* acetone-evaporated coatings considerably decelerated the evaporation of the droplet due to the enhanced evaporative cooling (Figure S9, Supporting Information).[82] The temporal evolution of the contact angle during the droplet evaporation on both surfaces shows a clear transition from relatively larger contact angles at early times (S_1), to an accelerated decrease to smaller contact angles at later times (S_2). This behavior was previously attributed to the transition from Cassie-Baxter to Wenzel state wetting, based on direct visualization.[83] Quantification of the local gradient of the contact line in time better highlights this adjustment in Figure 6 iii, indicative of a wetting regime transition. Assuming that the S_1 to S_2 transition during evaporation, highlighted in Figure 6b,i, iii, corresponds to the point at which full impalement occurs, Wenzel contact angles of 136 ± 2° and 123 ± 2° are derived for the acetone-evaporated and toluene-evaporate rice bran wax surfaces, respectively. The transition contact angle was found to be independent of the initial size for droplets of 1–10 µL volume (Figure S10, Supporting Information). The roughness factor *r*, defined as the ratio of the true contact area over the surface area, can be calculated in the Wenzel formulation $\mathrm{Cos}\,\theta_w = r\mathrm{Cos}\,\theta_0$, where θ_w is the Wenzel contact angle and θ_0 is the intrinsic contact angle of rice bran wax measured on coatings crystallized through cooling, see Figure 1. This was calculated to be $r_{\text{RB-acetone}} = 2.2$ and $r_{\text{RB-toluene}} = 1.7$ for coatings crystallized from acetone and toluene, respectively. The *r* factors calculated in the evaporation test are further corroborated by direct optical roughness analysis performed using LSCM,[84] yielding $r_{\text{RB-acetone}} = 2.3 \pm 0.7$ and $r_{\text{RB-toluene}} = 1.8 \pm 0.3$, when local surface roughness[85] was considered. See further details in Section S4.3 (Supporting Information).

The squeezing test resulted in full impalement of the droplet and transition to Wenzel regime on the toluene-evaporated surfaces with an equilibrium contact angle of 120 ± 4° (Figure 6b), in agreement with the value obtained in the evaporation test (Figure 6b). On acetone-evaporated coatings, however, squeezed water droplets detached entirely from the coating after the removal of the downward pressure, making it impossible to access the Wenzel regime through droplet squeezing. The combined findings of the squeezing and evaporation tests indirectly reveal that the acetone-evaporated surface exhibits true

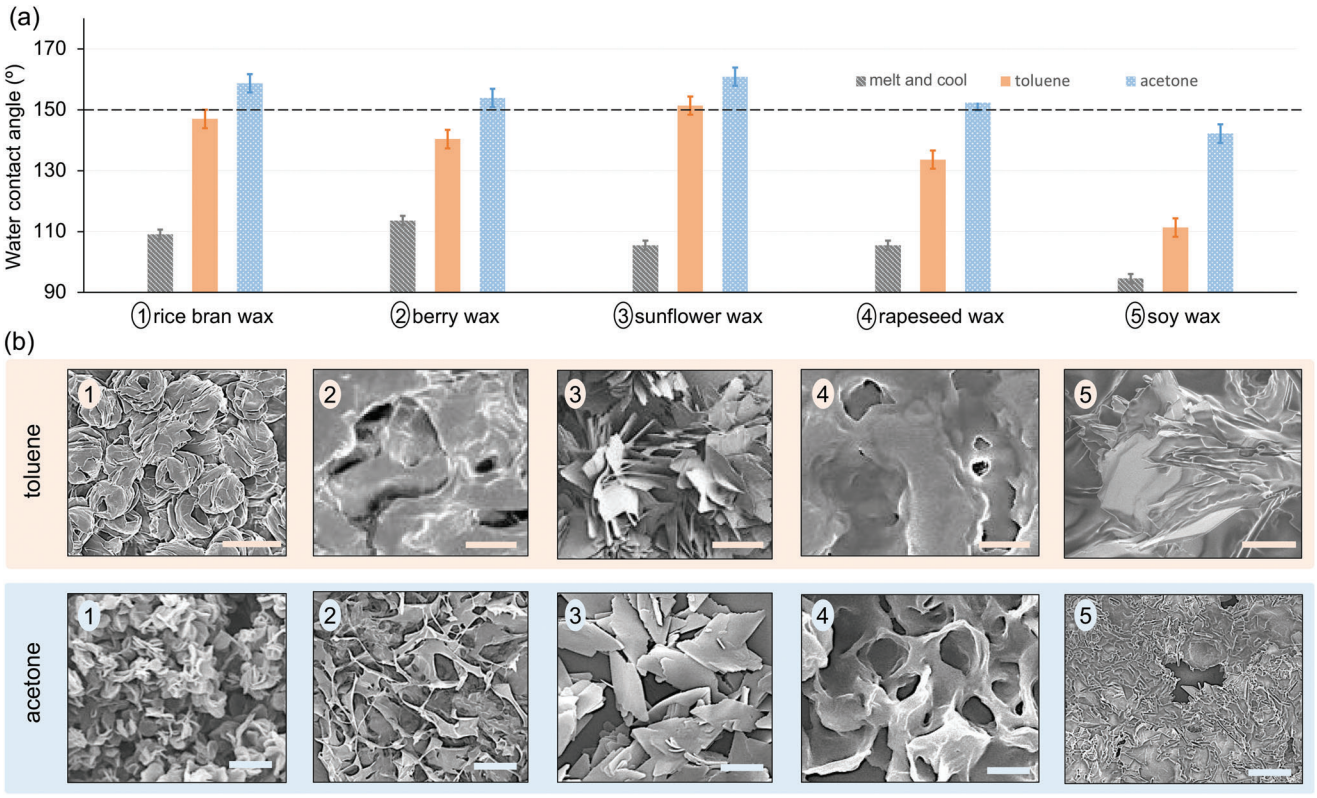

Figure 7. Surface wettability of morphologically diverse wax crystals. a) Static water contact angle measurements on coatings created through cooling wax melt and solvent evaporation for five different waxes. For all tested waxes, solvent evaporation induced surface roughness. Use of acetone resulted in enhanced surface hydrophobicity in comparison with toluene. b) SEM images of coatings generated through evaporation of toluene (top) and acetone (bottom). Scale bars in SEM images refer to 10 µm in all images.

Cassie-Baxter wetting, while the toluene-evaporated surface generates composite wetting behavior as suggested by Chakraborty et al.[23] the openings on the top of the micro-roses remain in the Cassie-Baxter regime while water partially penetrates the micro gap in between (Figure 6c).

2.4. Modulation of Crystal Micro-Structure in Alternative Plant Waxes

The role of solvent on the crystal topography and wetting behavior was also examined for the other plant-based waxes that were initially introduced in Figure 1. Topographic and wettability findings, represented in **Figure 7**, show general similarities with the rice bran wax coating results. Solvent evaporation in all waxes enhanced the surface hydrophobicity through the generation of 3D interfacial roughness, with dimensions ranging from hundreds of nanometres to a few micrometres. Using the fast-evaporating acetone generally led to smaller surface features (hundreds of nanometres), resulting in increased water contact angles in comparison to coatings obtained via toluene evaporation. Samples generated from the slow evaporation of toluene exhibited self-assembly of larger aggregates and *sticky* behavior. In contrast, the samples produced via the evaporation of acetone resulted in static water contact angles of $\geqslant 150°$ and smaller static siding angles ($3 \pm 1°$), with the exception of soy wax (Figure 7).

In the samples analyzed, rice bran, and sunflower waxes generated *rosettes* and *plates* when crystallized through the evaporation of acetone. These structures self-assembled into larger aggregates resembling microscopic flowers when toluene was used for crystallization. Toluene evaporation generated a *porous crust* in berry wax, whose edges opened up forming *membrane platelets* for acetone-evaporated samples.[72,86,87] The microscopic crystal morphologies in sunflower and berry wax crystallized from solutions in acetone resembled those obtained in the bulk solution.[88] Solvent evaporation created a porous *crust* in rapeseed wax surfaces, whose porosity significantly increased for acetone evaporation. Soy wax generated plates of 200–300 nm thickness when crystallized from solutions in acetone, while evaporation of toluene produced a nonhomogenous distribution of aggregated larger plates within the crust.

3. Conclusion

The crystalline structure produced via solvent evaporation yielded micro/nanoscale surface roughness with enhanced surface hydrophobicity for various waxes. The saturation level during the crystallization was found to impact the surface topographies and the water contact angle in both static and dynamic wetting regimes by regulating the crystallization kinetics. Using acetone as a fast-evaporating solvent resulted in superhydrophobic coatings with small rolling/sliding angles, while the slower

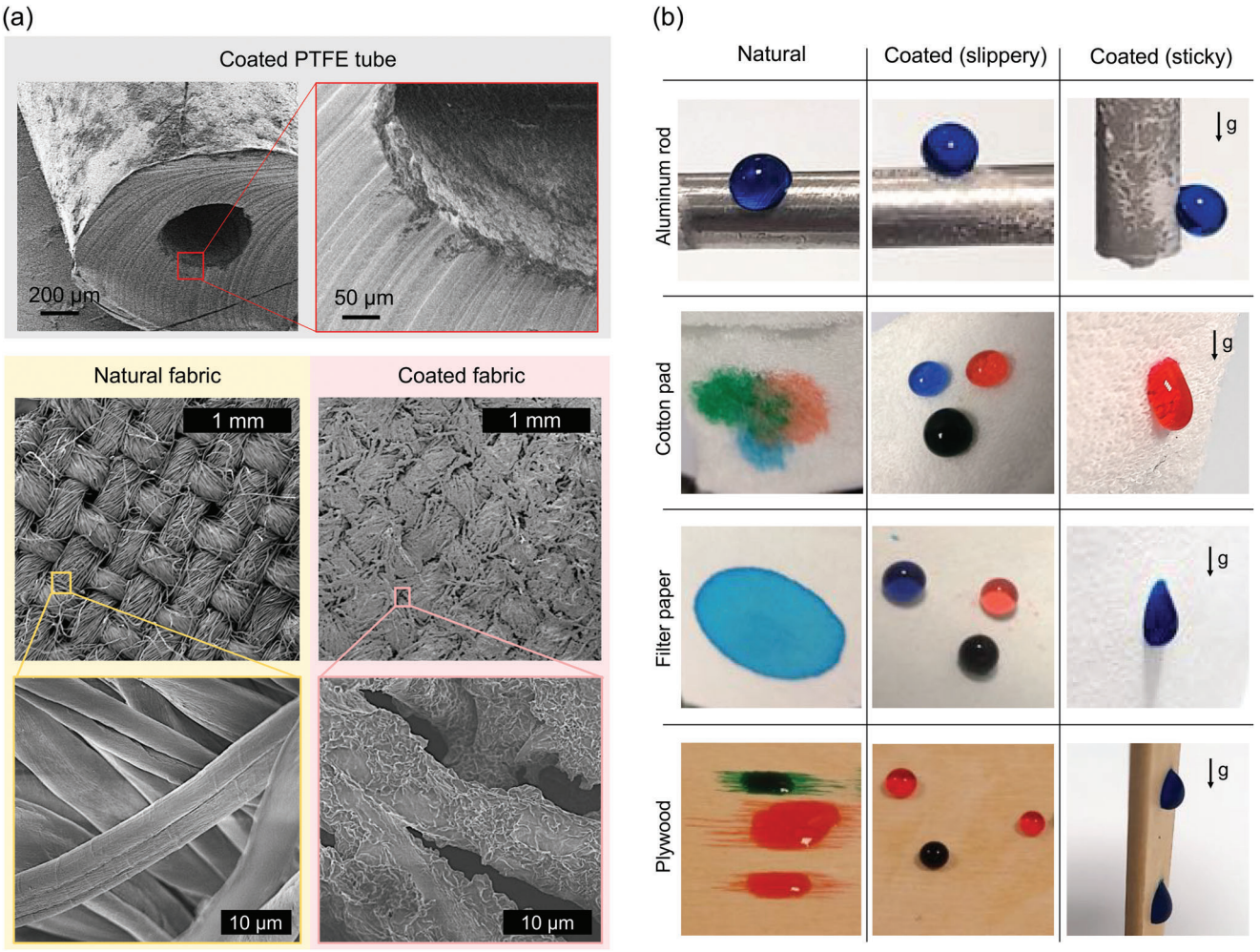

Figure 8. Wax crystallization for hydrophobic coating of curved interfaces and common porous materials. a) SEM images of (top) inner and outer walls of Polytetrafluoroethylene tube, and (bottom) woven fabric before and after coating. b) Wetting of dyed water droplets on natural and coated curved and porous surfaces. *Slippery* and *sticky* surfaces are generated using solutions of berry wax in acetone and toluene, respectively.

evaporation of toluene yielded large water contact angles with enhanced surface adhesion.

Plant-based waxes, especially those derived from oily seeds, have the potential for scalable fabrication of bio-degradable materials for various wetting and anti-wetting applications. While resistance to mechanical abrasion is limited for pure wax coatings with no additives, the simplicity of the approach is ideal for providing affordable superhydrophobic coatings for biodegradable single-use materials, packaging and devices.[62] Relying upon crystallization in initially isotropic solutions, the proposed technique is ideal for fluid transport applications that require water-repellent coatings of curved inner/outer walls and cavities in tubes and porous materials,[89,90] with examples demonstrated in **Figure 8**. The wide spectrum of phase change (melting) temperature, crystal morphology, and wettability modes of plant-based waxes provide opportunities for the large-scale fabrication of organic phase change materials (PCM)[91,92] and condensation units[54,93] in heat exchangers. Further, such single-step fluid-based manufacturing approaches can provide the base textured substrates for the encapsulation of oils in lubricant-infused slippery coatings on curved or confined surfaces. Besides the potential for surface manufacturing, understanding the link between the topography of plant-based wax crystals and surface wettability is of critical importance in the development of safe and effective agrochemical formulations.

4. Experimental Section

Materials: Several commercially available waxes were sourced from personal care, cosmetic, craft/decoration, and food additive suppliers and were used without further purification. Rice bran, sunflower, berry, rapeseed, and soy waxes were chosen for analysis due to their low surface energy (Figure 1) and solubility in lower risk-level solvents.[94] These waxes typically comprise lipid-based molecules containing long-chain fatty acid, alcohols and esters, the composition of which yields their water and polar liquid impermeability characteristics.[88,95,96] From a future application perspective, detailed characterizations in this study are primarily focused on rice bran wax due to its higher melting point and material accessibility as an industrial by-product.[63,97] Acetone (≥99.5%) and toluene (≥99.5%) were purchased from Avantor and used as received. Standard borosilicate

glass coverslips were used as substrates for all the presented wax-based coatings, unless otherwise indicated.

Methods — Fabrication of Wax-Based Coatings: Wax coatings were fabricated by drop-casting the dissolved wax solutions onto the glass substrate. An approximate 50 µL droplet of the solution was deposited upon contact onto the substrate and left to solidify at the stated conditions to form a thin film (Figure 2). The low surface tension of solvents in use ensured the spreading of the sessile droplet upon contact. For coatings crystallized via cooling, wax pellets were heated at temperatures above their melting points and left to cool at ambient laboratory conditions (24 ± 2°C). For solvent evaporation samples, waxes were initially dissolved in the solvent at 10 wt% using a magnetic stirrer on a hot plate set to 60–85°C, depending on the wax melting points. A wax concentration of 10 wt% was chosen as it provided full surface coverage and prevented additional vertical stacking of crystals (Figure S1, Supporting Information). The drop-casted samples were left to crystallize at the same ambient laboratory conditions for at least 48 hours to ensure complete solvent evaporation. The impact of *casting temperature*, presented in Figure 3, was studied on a temperature-controlled glass substrate, using a Peltier device.

Methods — Analytical Characterization: Crystal structures were analyzed by X-ray diffraction (XRD), using a Bruker D8 diffractometer with monochromatic Cu Kα radiation (2θ range 2°–70°, step size = 0.03°). Differential Scanning Calorimetry (DSC) was used to measure the respective melting and crystallization temperatures of the rice bran wax samples with further details of operation cycles in Figure S2 (Supporting Information). Solid crystals were collected from the surface after cooling or solvent evaporation for XRD and DSC analyses. Attenuated total reflection (ATR) analysis with Fourier transform infrared spectroscopy (FTIR) was performed directly on the wax coating using the diamond crystal (Platinum ATR accessory) to compare the respective chemical compounds. The infrared spectra were recorded using a Bruker Tensor 27 System with DTGS detector. For each spectrum, 64 single beam scans were averaged with 4 cm^{-1} resolution in the range of 4000–600 cm^{-1}. The clean, dry diamond crystal was consistently used for background correction. Results were examined in the absorbance unit using OPUS software with no further data processing.

Methods — Topography Characterization: Images of wax crystals were captured on gold-coated samples using scanning electron microscopy (SEM) on a Zeiss EVO MA15 microscope operated at 20 kV accelerating voltage. Higher resolution images were obtained on a Hitachi SU8230 SEM operated at 2.0 kV accelerating voltage from samples sputter coated with 10 nm of Iridium. To obtain quantitative surface roughness measurements, laser scanning confocal microscopy (LSCM) was performed over a larger scan area ($\geqslant$50 µm) using a Zeiss LSM800 equipped with a 405 nm laser.

Methods — Wetting Characterization: Comprehensive wetting characterization of the rice bran wax samples was completed by analysing the static and dynamic contact angles of de-ionized water droplets on the surface of the coatings. Static contact angle measurements were performed using a customized micro-imaging setup and the drop analysis plugin on ImageJ.[98] The average value of the left and right static contact angles were analyzed for each droplet. For every condition, five independent coatings were tested. On each coated surface, the average contact angle was calculated for three droplets to account for surface non-homogeneity. Error bars on all presented graphs correspond to the standard deviation of the mean values. Sliding angles of water droplets on coated surfaces were measured by increasing the base angle using a manual goniometer stage with an uncertainty of $\pm$0.5°. Reported static and dynamic angles were measured for droplets of 1–2 mm diameter. Evaporating droplets of different sizes were studied on the fabricated wax surfaces in ambient laboratory conditions using an automated optical tensiometer setup (Theta, Biolin Scientific) in shadowgraphy mode. During droplet evaporation, images were captured and analyzed to attain contact angle, volume and baseline length of the sessile droplets with respect to time to elucidate the hydrophobic wetting states. Further droplet squeezing tests were performed to visualize and characterize the different wetting states and the transition between them. A sessile droplet of 5 µL volume was placed onto the wax coating and compressed from the top by a flat hydrophobic surface until a minimum gap of 0.5 mm between the surfaces was reached.

Supporting Information

Supporting Information is available from the Wiley Online Library or from the author.

Acknowledgements

F.D. was supported by the Engineering and Physical Sciences Research Council through the EPSRC Collaborative Studentship program (EP/T517860/1). S.K. was supported by The Wellcome Trust Institutional Strategic Support Fund (ISSF, 204825/Z/16/Z) and The Royal Society Research Grant (RGS\R1\211265). The authors thank Stuart Micklethwaite at Leeds Electron Microscopy and Spectroscopy Centre (LEMAS), Karin Alves Thorne and Adrian Cunliffe for their support with SEM imaging and DSC analyses.

Conflict of Interest

The authors declare no conflict of interest.

Data Availability Statement

The data that support the findings of this study are available from the corresponding author upon reasonable request.

Keywords

coating, hydrophobic, plant-based, surface roughness, topography, wax, wetting

Received: July 12, 2023
Revised: August 28, 2023
Published online: September 19, 2023

[1] E. Vazirinasab, R. Jafari, G. Momen, *Surf. Coat. Technol.* **2018**, *341*, 40.
[2] E. J. Falde, S. T. Yohe, Y. L. Colson, M. W. Grinstaff, *Biomaterials* **2016**, *104*, 87.
[3] D. Quéré, *Rep. Prog. Phys.* **2005**, *68*, 2495.
[4] T. Onda, S. Shibuichi, N. Satoh, K. Tsujii, *Langmuir* **1996**, *12*, 2125.
[5] X.-M. Li, D. Reinhoudt, M. Crego-Calama, *Chem. Soc. Rev.* **2007**, *36*, 1350.
[6] D. Quéré, *Ann. Rev. Mater. Res.* **2008**, *38*, 71.
[7] S. Parvate, P. Dixit, S. Chattopadhyay, *J. Phys. Chem. B* **2020**, *124*, 1323.
[8] D. Wang, Q. Sun, M. J. Hokkanen, C. Zhang, F.-Y. Lin, Q. Liu, S.-P. Zhu, T. Zhou, Q. Chang, B. He, Q. Zhou, L. Chen, Z. Wang, R. H. A. Ras, X. Deng, *Nature* **2020**, *582*, 55.
[9] A. Lafuma, D. Quéré, *Nat. Mater.* **2003**, *2*, 457.
[10] N. J. Shirtcliffe, G. McHale, S. Atherton, M. I. Newton, *Adv. Colloid Interf. Sci.* **2010**, *161*, 124.
[11] R. N. Wenzel, *Ind. Eng. Chem.* **1936**, *28*, 988.
[12] G. McHale, N. J. Shirtcliffe, M. I. Newton, *Langmuir* **2004**, *20*, 10146.
[13] D. Quéré, A. Lafuma, J. Bico, *Nanotechnol.* **2003**, *14*, 1109.
[14] D. Quéré, *Nat. Mater.* **2002**, *1*, 14.
[15] J. Bico, C. Marzolin, D. Quéré, *Europhys. Lett.* **1999**, *47*, 220.
[16] A. B. D. Cassie, S. Baxter, *Trans. Faraday Soc.* **1944**, *40*, 546.
[17] B. Bhushan, Y. C. Jung, K. Koch, *Philos. T. R. Soc. A* **2009**, *367*, 1631.
[18] T.-m. Cai, Z.-h. Jia, H.-n. Yang, G. Wang, *Colloid Polym. Sci.* **2016**, *294*, 833.

[19] B. Bhushan, E. K. Her, *Langmuir* **2010**, *26*, 8207.
[20] K.-H. Cho, L.-J. Chen, *Nanotechnol.* **2011**, *22*, 445706.
[21] X. Dai, B. B. Stogin, S. Yang, T.-S. Wong, *ACS Nano* **2015**, *9*, 9260.
[22] M. Cao, J. Xiao, C. Yu, K. Li, L. Jiang, *Small* **2015**, *11*, 4379.
[23] M. Chakraborty, J. A. Weibel, J. A. Schaber, S. V. Garimella, *Adv. Mater. Interf.* **2019**, *6*, 1900652.
[24] E. Celia, T. Darmanin, E. Taffin de Givenchy, S. Amigoni, F. Guittard, *J. Colloid Interf. Sci.* **2013**, *402*, 1.
[25] C. R. Szczepanski, F. Guittard, T. Darmanin, *Adv. Colloid Interf. Sci.* **2017**, *241*, 37.
[26] I. S. Bayer, *Adv. Mater. Interf.* **2020**, *7*, 2000095.
[27] J. M. Morrissette, P. J. Carroll, I. S. Bayer, J. Qin, D. Waldroup, C. M. Megaridis, *Green Chem.* **2018**, *20*, 5169.
[28] M. Ghasemlou, F. Daver, E. P. Ivanova, B. Adhikari, *J. Mater. Chem. A* **2019**, *7*, 16643.
[29] J. Peng, L. Wu, H. Zhang, B. Wang, Y. Si, S. Jin, H. Zhu, *Chem. Commun.* **2022**, *58*, 11236.
[30] A. Goralczyk, S. Savicheva, R. Montazeri, S. Fine, F. Mayoussi, P. Zhu, K. Steffen, F. Kotz-Helmer, D. Helmer, B. E. Rapp, *Adv. Eng. Mater.* **2023**, *25*, 2201314.
[31] F. J. Dent, D. Harbottle, N. J. Warren, S. Khodaparast, *Soft Matter* **2023**, *19*, 2737.
[32] W. Barthlott, M. Mail, C. Neinhuis, *Philos. T. R. Soc. A* **2016**, *374*, 20160191.
[33] K. Koch, H.-J. Ensikat, *Micron.* **2008**, *39*, 759.
[34] K. Koch, B. Bhushan, W. Barthlott, *Prog. Mater. Sci.* **2009**, *54*, 137.
[35] W. Barthlott, C. Neinhuis, *Planta* **1997**, *202*, 1.
[36] W. Barthlott, M. Mail, B. Bhushan, K. Koch, *Nano-Micro Lett.* **2017**, *9*, 23.
[37] P. J. Holloway, *Ann. Appl. Biol.* **1969**, *63*, 145.
[38] H. J. Ensikat, P. Ditsche-Kuru, C. Neinhuis, W. Barthlott, *Beilstein J. Nanotechnol.* **2011**, *2*, 152.
[39] C. E. Jeffree, E. A. Baker, P. J. Holloway, *New Phytol.* **1975**, *75*, 539.
[40] J. Jetter, M. Riederer, *Planta* **1994**, *195*, 257.
[41] K. Koch, W. Barthlott, S. Koch, A. Hommes, K. Wandelt, W. Mamdouh, S. De-Feyter, P. Broekmann, *Planta* **2006**, *223*, 258.
[42] B. Bhushan, Y. C. Jung, A. Niemietz, K. Koch, *Langmuir* **2009**, *25*, 1659.
[43] K. Koch, A. Dommisse, W. Barthlott, *Cryst. Growth Des.* **2006**, *6*, 2571.
[44] V. S. Saji, *Colloid Surf. A* **2020**, *602*, 125132.
[45] I. S. Bayer, D. Fragouli, P. J. Martorana, L. Martiradonna, R. Cingolani, A. Athanassiou, *Soft Matter* **2011**, *7*, 7939.
[46] W. Zhang, P. Lu, L. Qian, H. Xiao, *Chem. Eng. J.* **2014**, *250*, 431.
[47] S. Beluns, O. Platnieks, J. Sevcenko, M. Jure, G. Gaidukova, L. Grase, S. Gaidukovs, *Membranes* **2022**, *12*, 5.
[48] A. Niemietz, K. Wandelt, W. Barthlott, K. Koch, *Prog. Org. Coat.* **2009**, *66*, 221.
[49] S. Pechook, B. Pokroy, *Adv. Func, Mater.* **2012**, *22*, 745.
[50] X. Gao, L. Jiang, *Nature* **2004**, *432*, 36.
[51] L. Feng, Y. Zhang, J. Xi, Y. Zhu, N. Wang, F. Xia, L. Jiang, *Langmuir* **2008**, *24*, 4114.
[52] Q. Wang, X. Yao, H. Liu, D. Quéré, L. Jiang, *P. Natl. A. Sci.* **2015**, *112*, 9247.
[53] T. Nørgaard, M. Dacke, *Front. Zool.* **2010**, *7*, 23.
[54] C. S. Sharma, C. Stamatopoulos, R. Suter, P. R. von Rohr, D. Poulikakos, *ACS Appl. Mater. Interf.* **2018**, *10*, 29127.
[55] W. Kim, J. Eun, S. Jeon, *Appl. Surf. Sci.* **2021**, *542*, 148617.
[56] S. Khodaparast, F. Boulogne, C. Poulard, H. A. Stone, *Phys. Rev. Lett.* **2017**, *119*, 154502.
[57] Z. Guo, W. Liu, *Plant Sci.* **2007**, *172*, 1103.
[58] B. Bhushan, M. Nosonovsky, *Philos. T. R. Soc. A* **2010**, *368*, 4713.
[59] D. Zheng, Y. Jiang, W. Yu, X. Jiang, X. Zhao, C.-H. Choi, G. Sun, *Langmuir* **2017**, *33*, 13640.
[60] J. Li, Z. Guo, W. Liu, *Adv. Mater. Interf.* **2023**, *10*, 2201847.
[61] R. T. Vaclav Šprdlík, V. Kotradyová, *BioResources* **2017**, *12*, 2.
[62] X. Zhao, T. Hu, J. Zhang, *J. Colloid Interf. Sci.* **2018**, *515*, 255.
[63] L. S. K. Dassanayake, D. R. Kodali, S. Ueno, K. Sato, *J. Am. Oil Chem. Soc.* **2009**, *86*, 1163.
[64] H. Ensikat, M. Boese, W. Mader, W. Barthlott, K. Koch, *Chem. Phys. Lipids* **2006**, *144*, 45.
[65] D. W. Jennings, K. Weispfennig, *Fluid Phase Equilibr.* **2005**, *227*, 27.
[66] A. E. Nielsen, *Krist Tech.* **1969**, *4*, 17.
[67] N. W. Krase, J. B. Goodman, *Ind. Eng. Chem.* **1930**, *22*, 13.
[68] D. M. Croker, D. M. Kelly, D. E. Horgan, B. K. Hodnett, S. E. Lawrence, H. A. Moynihan, Å. C. Rasmuson, *Org. Process Res. Dev.* **2015**, *19*, 1826.
[69] D. Bosse, H.-J. Bart, *Ind. Eng. Chem. Res.* **2005**, *44*, 8873.
[70] D. Bartolo, F. Bouamrirene, É. Verneuil, A. Buguin, P. Silberzan, S. Moulinet, *Europhys. Lett.* **2006**, *74*, 299.
[71] D. Richard, D. Quéré, *Europhys. Lett.* **2000**, *50*, 769.
[72] P. J. Holloway, *Pestic. Sci.* **1970**, *1*, 156.
[73] T. E. Dawson, G. R. Goldsmith, *New Phytol.* **2018**, *219*, 1156.
[74] A.-K. Lenz, U. Bauer, G. D. Ruxton, *J. Exp. Bot.s* **2021**, *73*, 1176.
[75] X. Sun, V. G. Damle, S. Liu, K. Rykaczewski, *Adv. Mater. Interf.* **2015**, *2*, 1400479.
[76] X. Zhou, Y. Sun, J. Liu, *Adv. Mater. Interf.* **2021**, *8*, 2100327.
[77] J. A. Zabkiewicz, *Crop Prot.* **2007**, *26*, 312.
[78] S. Wang, L. Jiang, *Adv. Mater.* **2007**, *19*, 3423.
[79] H. Zhu, Z. Guo, *J. Bionic Eng.* **2016**, *13*, 213.
[80] H. Y. Erbil, *Adv. Colloid Interf. Sci.* **2012**, *170*, 67.
[81] X. Zhang, S. Tan, N. Zhao, X. Guo, X. Zhang, Y. Zhang, J. Xu, *ChemPhysChem.* **2006**, *7*, 2067.
[82] Z. Pan, S. Dash, J. A. Weibel, S. V. Garimella, *Langmuir* **2013**, *29*, 15831.
[83] P. Tsai, R. G. H. Lammertink, M. Wessling, D. Lohse, *Phys. Rev. Lett.* **2010**, *104*, 116102.
[84] A. Hongru, L. Xiangqin, S. Shuyan, Z. Ying, L. Tianqing, *RSC Adv.* **2017**, *7*, 7052.
[85] M. Nosonovsky, *Langmuir* **2007**, *23*, 9919.
[86] W. Barthlott, C. Neinhuis, D. Cutler, F. Ditsch, I. Meusel, I. Theisen, H. Wilhelmi, *Bot. J. Linn. Soc.* **1998**, *126*, 237.
[87] K. Koch, B. Bhushan, W. Barthlott, *Soft Matter* **2008**, *4*, 1943.
[88] C. D. Doan, I. Tavernier, M. D. B. Sintang, S. Danthine, D. Van de Walle, T. Rimaux, K. Dewettinck, *Food Biophys.* **2017**, *12*, 97.
[89] Y. Hou, Z. Wang, J. Guo, H. Shen, H. Zhang, N. Zhao, Y. Zhao, L. Chen, S. Liang, Y. Jin, J. Xu, *J. Mater. Chem. A* **2015**, *3*, 23252.
[90] S. Hoshian, E. Kankuri, R. H. A. Ras, S. Franssila, V. Jokinen, *Sci. Rep.* **2017**, *7*, 16019.
[91] S. Kahwaji, M. B. Johnson, A. C. Kheirabadi, D. Groulx, M. A. White, *Energy* **2018**, *162*, 1169.
[92] A. R. Vakhshouri, *Paraffin as Phase Change Material*, Ch. 5, IntechOpen, Rijeka, ISBN 978-1-83880-595-1, **2019**.
[93] R. Gulfam, T.-e. Huang, C. Lv, D. Orejon, P. Zhang, *Int. J. Heat Mass Tran.* **2022**, *185*, 122384.
[94] M. Tobiszewski, J. Namieśnik, F. Pena-Pereira, *Green Chem.* **2017**, *19*, 1034.
[95] P. Podchong, K. Aumpai, S. Sonwai, D. Rousseau, *Food Chem.* **2022**, *397*, 133635.
[96] M. C. Agogué, C. Loisel, O. Gonçalves, J. Legrand, S. Saint-Jalmes, A. Arhaliass, *J. Am. Oil Chem. Soc.* **2022**, *99*, 1137.
[97] M. K. Sharif, M. S. Butt, F. M. Anjum, S. H. Khan, *Crit. Rev. Food. Sci. Nutr.* **2014**, *54*, 807.
[98] A. F. Stalder, G. Kulik, D. Sage, L. Barbieri, P. Hoffmann, *Colloid Surf. A* **2006**, *286*, 92.